SOFT ROBOTS

Biohybrid soft robots with self-stimulating skeletons

Maria Guix[1]*†, Rafael Mestre[1]†, Tania Patiño[1,2], Marco De Corato[1], Judith Fuentes[1], Giulia Zarpellon[1], Samuel Sánchez[1,3]*

Bioinspired hybrid soft robots that combine living and synthetic components are an emerging field in the development of advanced actuators and other robotic platforms (i.e., swimmers, crawlers, and walkers). The integration of biological components offers unique characteristics that artificial materials cannot precisely replicate, such as adaptability and response to external stimuli. Here, we present a skeletal muscle–based swimming biobot with a three-dimensional (3D)–printed serpentine spring skeleton that provides mechanical integrity and self-stimulation during the cell maturation process. The restoring force inherent to the spring system allows a dynamic skeleton compliance upon spontaneous muscle contraction, leading to a cyclic mechanical stimulation process that improves the muscle force output without external stimuli. Optimization of the 3D-printed skeletons is carried out by studying the geometrical stiffnesses of different designs via finite element analysis. Upon electrical actuation of the muscle tissue, two types of motion mechanisms are experimentally observed: directional swimming when the biobot is at the liquid-air interface and coasting motion when it is near the bottom surface. The integrated compliant skeleton provides both the mechanical self-stimulation and the required asymmetry for directional motion, displaying its maximum velocity at 5 hertz (800 micrometers per second, 3 body lengths per second). This skeletal muscle–based biohybrid swimmer attains speeds comparable with those of cardiac-based biohybrid robots and outperforms other muscle-based swimmers. The integration of serpentine-like structures in hybrid robotic systems allows self-stimulation processes that could lead to higher force outputs in current and future biomimetic robotic platforms.

INTRODUCTION

Biological systems have evolved throughout millennia to develop sophisticated mechanisms of self-organization (*1*), actuation (*2*), self-healing (*3*), and sensing (*4*). The robotics field aims to mimic and incorporate these complex behaviors (*5*–*8*). In the field of biomimetic soft robots, recent developments in material science enabled the fabrication of systems able to perform some simple types of actuation (*9*), including crawling (*10*, *11*) or grasping (*12*), but they are still far from the degree of complexity, sophistication, and potential scalability toward small dimensions of their biological counterparts. One of the most investigated applications in soft robotics is the development of artificial muscles that can mimic the performance of native muscle tissue (*13*, *14*). However, materials of synthetic origin still lack the ability to fully replicate the complexity and force output arising from the hierarchical organization of muscle tissue. To address the challenges of achieving the inherent mechanical properties (i.e., compliance and flexibility) and sensing capabilities from the native muscle, biohybrid robotics proposes a synergistic strategy to integrate the best characteristics of biological entities (i.e., self-healing, adaptability, and sensing) and artificial materials for obtaining more efficient and complex systems (*15*, *16*).

Biohybrid robots or biobots are generally composed of muscle tissue, either cardiac or skeletal, and an artificial scaffold. In the past two decades, many of the fabricated biobots have been based on thin film structures [i.e., microelectromechanical systems (MEMS), polydimethylsiloxane (PDMS), and other elastomeric or nonelastomeric materials] seeded with cardiac or skeletal muscle cells (*17*–*27*), promoting a two-dimensional (2D) layer configuration that has been extensively explored for fish-like swimming purposes (*28*, *29*). Some examples include a swimming biohybrid soft robotic stingray based on optogenetically modified cardiac cells (*30*) and a cardiac-based medusoid that mimics the thrusting mechanism of a jellyfish (*31*). However, recent advances in both 3D printing (*32*) and tissue engineering (*33*) have allowed the creation of on-demand 3D biological structures, instead of relying on 2D layer configurations, paving the way to their integration in smart soft robotic platforms.

Skeletal muscle–based biobot actuations rely mostly on actuators or walkers (*34*, *35*). Some of the earliest skeletal muscle biohybrid systems were tethered, owed their actuation to the deflection of cantilevers by the muscle tissue (*36*–*40*), and used as grippers (*34*, *41*). However, in untethered biohybrid robots, crawling has been the main described motion mechanism (*42*). In addition, whereas cardiac cells present spontaneous contractions whose response can be stimulated and synchronized at a certain frequency but cannot be stopped, skeletal muscle tissue has a wider range of adaptability and controllability, because these cells adopt a 3D structure that can be accommodated to different substrates and their contractions are induced on demand by means of an external electrical or optical stimulus (*43*, *44*). In addition, self-healing (*45*), adaptability (*44*), integration of motor neurons for advanced stimulation (*46*), long-time preservation (*47*, *48*), scalability (*49*), and their integration with microelectrodes (*50*) were demonstrated for skeletal muscle biohybrid robots. The integration of neuronal and skeletal muscle tissue in one single biobot has been of great interest, because it resembles the structure of native muscle to obtain improved controllability of the biorobotic systems (*51*, *52*). In this regard, a biohybrid swimmer with functional neuromuscular junction

---

[1] Institute for Bioengineering of Catalonia (IBEC), Barcelona Institute of Science and Technology (BIST), Baldiri-Reixac 10-12, 08028 Barcelona, Spain. [2] Chemistry Department, University of Rome, Tor Vergata, Via della Ricerca Scientifica, 00133 Rome, Italy. [3] Institució Catalana de Recerca i Estudis Avançats (ICREA), Passeig de Lluís Companys 23, 08010 Barcelona, Spain.
*Corresponding author. Email: ssanchez@ibecbarcelona.eu (S.S.); mguix@ibecbarcelona.eu (M.G.)

†These authors contributed equally to this work.

that swims with time-irreversible flagellar dynamics has recently been reported (*53*). This biobot configuration represents the first swimmer based on skeletal muscle tissue, whose actuation relies on external light stimuli, and it presents slow swimming speeds (0.92 μm/s) when moving at a low Reynolds number regime.

Although several aspects concerning skeletal muscle–based biobot controllability and scalability had been explored, it is important to find alternative efficient motion mechanisms to develop faster and more dynamic robotic designs. Here, we report a skeletal muscle–based swimming biobot with enhanced force performance and directional motion. The integration of a serpentine spring skeleton into the biobot platform provides more mechanical integrity to the whole system, as well as mechanical self-stimulation due to the spring restoring force when spontaneous contractions take place during the cell maturation process. This self-training event leads to enhanced actuation and larger contraction force in the biobot performance. This biobot is based on a 3D skeletal muscle structure instead of 2D thin films as used in previous cardiomyocyte- and skeletal muscle–based biohybrid swimmers mentioned above, offering a wider range of customization and actuation modes. Furthermore, the 3D serpentine spring structure that forms the compliant skeleton has been designed to present asymmetric stiffness throughout its structure, leading to a well-controlled bending of the biobot that permits two different motion modalities: (i) swimming when located at the air-liquid interface and (ii) coasting when it is placed near the bottom surface. Corresponding motion mechanisms were established by motion tracking and simulations of the locomotion hydrodynamics, revealing that the asymmetry in geometrical stiffness provides directional motion for the swimming case. Our biobot design is the fastest skeletal muscle–based swimming biohybrid robot to date by several orders of magnitude (791×; Fig. 1), and its velocity compares favorably with biorobotic systems based on cardiac cells (for comparison, see Fig. 1). The integration of a serpentine spring on a biorobotic platform serves both as a compliant skeleton useful for mechanical self-stimulation purposes and to provide asymmetry to the system. Thus, its potential for a greater differentiation and better performance when compared with nondynamic cell-actuated robotic platforms is demonstrated. Our approach may inspire future biohybrid robotic designs with higher efficiency and enabling the opportunity for more complex motion patterns.

RESULTS

Skeletal muscle–based biobots with an integrated spring-like skeleton were constructed by assembling a cell-laden circular hydrogel around the compliant skeleton (Fig. 2A). The skeleton was composed of PDMS and created by extrusion-based 3D printing (Fig. 2B). The use of the 3D-printing technique provided high versatility and fast prototyping, allowing the design and optimization of different configurations of the artificial skeleton. The main configurations considered were a symmetric (Fig. 2C1) and an asymmetric (Fig. 2C2) design, the latter including a small post bulging out of one of the sides. This element induced an asymmetric compaction of the skeleton of the biobot, necessary to achieve directional motion. Not only was the overall stiffness of the skeleton tuned by varying the curing agent–to–base ratio of PDMS, but also an extra level of optimization was assessed by modifying its geometrical stiffness. Therefore, different serpentine designs in the central part of the biobot skeleton were considered and further evaluated (Fig. 2C3). A rounded notch was included at both ends of the skeleton, being carefully designed and 3D-printed (Fig. 2C4) to hold the tissue ring in place and avoid its release during the maturation process or their motion evaluation. Last, further optimization could be achieved by including different numbers of coils in the design to create biobots with different properties and sizes (Fig. 2C5). Although the shorter skeleton design did not provide enough flexibility to the system, the design with higher number of coils led to a nonstable assembly of the scaffold to the skeleton due to its large bending at earlier stages. The optimal two-coil configuration, however, allowed an optimal balance between the restoring force and the biobot stability during the maturation process and later motion studies.

Regarding the active biological muscle–based actuator, the cell-laden scaffold was prepared by using customized 3D-printed molds with the desired circular shape and size. A hydrogel composed of fibrinogen, thrombin, and Matrigel and laden with skeletal muscle myoblasts was cast inside the mold (Fig. 2D), leaving the whole setup first in growth medium (GM) to let the cells grow and expand and later on in differentiation medium (DM) to allow the differentiation process (*42*). Both GM and DM were supplemented with 6-aminocaproic acid (ACA) to reduce the degradation of the hydrogel due to proteases (*47*). The cross-linking of the hydrogel was studied over time to closely evaluate the gelation process and obtain reproducible cell-laden scaffolds for the biobot construction. Figure 2D shows the shear storage and loss moduli of the hydrogel at 37°C at a frequency of 1 Hz for 90 min. At the start of the characterization, when fibrinogen, thrombin, and Matrigel have been mixed, an initial peak in both moduli after 5 min points at the fast cross-linking of fibrinogen into fibrin by the action of the enzyme thrombin. After about 30 min at physiological temperatures, another increase in the absolute value of the shear modulus indicates the thermal-induced cross-linking of Matrigel. After this point, the structure of the cell-laden hydrogel is stable, and warm GM can be added to the injection mold for cell culture.

The preparation and maturation process of the skeletal muscle biobot comprises several stages. Figure 3 depicts the process timeline to obtain a myoblast-laden hydrogel. In stage 1, C2C12 cells are embedded in the 3D scaffold and left to grow for 3 days, leading to a myoblast-laden hydrogel. The hydrogel composition was adapted from Raman *et al.* (*42*), using a fibrinogen (4 mg/ml) and 30% (v/v) Matrigel concentration, which has been reported to be the ideal concentrations for optimal muscle performance (*54*). The cell-laden scaffold is manually transferred to the 3D-printed compliant skeleton based on PDMS in the presence of DM (stage 2). At this point, insulin-like growth factor (IGF-1) present in the solution promotes the fusion and differentiation of myoblast into myotubes (*35*), supporting the differentiation process and leading to the natural compaction of the muscle actuator around the compliant skeleton. During the maturation process, the cell-laden scaffold will perfectly adapt to the skeleton's shape thanks to the rounded edges, avoiding the formation of stresses that could damage the tissue. Due to these compaction forces and to the rounded notches that prevent disassembly, the biobot adopts a buckling structure that provides the necessary asymmetry to the biobot's conformation for optimal motion (stage 3).

The compliant mechanism of our untethered biohybrid robot is based on the longitudinal force exerted along the beam axis by the muscle tissue around the serpentine-like skeleton upon electrical pulse stimulation (EPS) (Fig. 3B). The compliant nature of the

Bio-robot/Mechanism	**Size [mm]**	**Speed [mm/min]**	**Relative speed [Body length/min]**	**Schematic**
Cardiomyocytes cells assembled to a MEMS system *(17)* *Swimming*	0.612	2.28	3.72	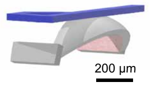
Spatially ordered **cardiomyocytes** on PDMS thin films *(18)* *Swimming*	6	20	3.33	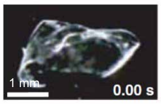
Cardiomyocytes seeded onto a PDMS thin layer consisting of 3 strips *(19)* *Walking*	2	6	3	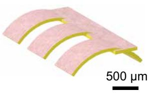
Cardiomyocytes cell monolayer onto flexible elastomer *(31)* *Swimming*	6	71.53	11.9	
Cardiomyocytes seeded on a PDMS cantilever structure *(20)* *Walking*	7	14.16	2	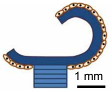
3D-printed **skeletal muscle**-based hydrogel assembled to flexible asymmetric skeleton *(44)* *Crawling*	5.5	9.36	1.5	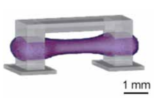
Cardiomyocytes patterned onto elastomeric ray-like structure *(30)* *Swimming*	14	90	6.42	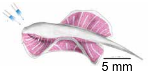
Computational design of 3D-printed **skeletal muscle**-based hydrogel with tissue bridging the pillars from the skeleton *(49)* *Crawling*	13.6	30	2.20	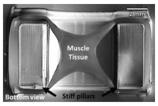
Free-standing soft scaffold assembled to **skeletal muscle** tissue and on-board neuromuscular units *(53)* *Swimming*	3	0.042	0.014	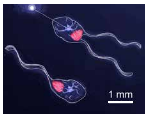
Skeletal muscle-based tissue assembled to PDMS-based serpentine spring – this work *Swimming*	12	33.24	2.77	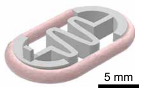

Fig. 1. Chronological summary of biohybrid robotic system development based on cardiac and muscular cells, indicating their size, real and relative speed (body lengths per second), and the corresponding schematic. Size value corresponds to the larger biobot dimension, being the length or the width, depending on each design. Image credits: second from top, reprinted with permission from (*18*) (copyright 2007 AAAS); fifth from the top, (*20*); sixth from the top, www.youtube.com/watch?v=skCzl7FlM34; seventh from the top, reprinted with permission from (*30*) (copyright 2016 AAAS); eighth from the top, reprinted with permission from (*49*) (copyright 2018 Wiley-VCH); ninth from the top, (*53*).

spring serpentine structure allows its deformation with low geometrical stiffness and a restoring force that brings the biobot back to its original state.

The skeleton optimal geometrical parameters were evaluated by using finite element analysis (FEA). To study the effect of the spring design on the compression efficiency, we designed three different geometries: (i) case 1, with a low-degree variation along the serpentine, creating low-amplitude oscillations; (ii) case 2, with much larger amplitude in the oscillations, allowing a better distribution of the stresses; and (iii) case 3, with large amplitude but a strict 180° angle at the points of curvature (Fig. 4A). To mimic the compression from the skeletal muscle tissue contraction on the compliant skeleton, two uniaxial point forces of the same magnitude were applied at both sides of the structure in a 3D simulation (assuming static conditions and only mechanical and linear deformations). The profile of a real twitch contraction was measured by image difference and was normalized in a way that the maximum value was 100 μN (more details in the Supplementary Materials) for a more meaningful simulation of the contraction kinetics. On the right side of Fig. 4A, we calculated the von Mises stresses of each skeleton case for a compression force of 100 μN. The von Mises stress is used to predict yielding of materials under complex loading from the results obtained from uniaxial tensile test and provides information about the equivalent stress distribution across the whole structure. The higher and localized stress values obtained for cases 2 and 3 already indicate that these structures can probably compress easier than case 1, although a better characterization of this can be obtained by calculating the geometrical stiffness of the designs.

The geometric stiffness of the skeletons is a parameter that gives information about the stiffness of the material after applying a deformation, taking only into consideration the geometry of the structure. For each design, we performed a force sweep using the contraction profile with a maximum force in the range of 10 to 100 μN (symmetrically at both edges), based on reported forces in the literature (*35*, *43*). The maximum uniaxial compression of the compliant skeleton, which coincided in time with the maximum force of the contraction profile, was plotted in terms of the force (left top side, Fig. 4A), revealing a linear elastic response dictated by Hooke's law, that allowed us to calculate the geometrical stiffness of the material, k, by the equation $F = kx$, where F is the applied force and x is the compression. The inverse of the slope yields the geometrical stiffnesses (left bottom side, Fig. 4A), where we can see that case 1, with a soft curvature in its coil, had much larger geometrical stiffness than the other two cases, which

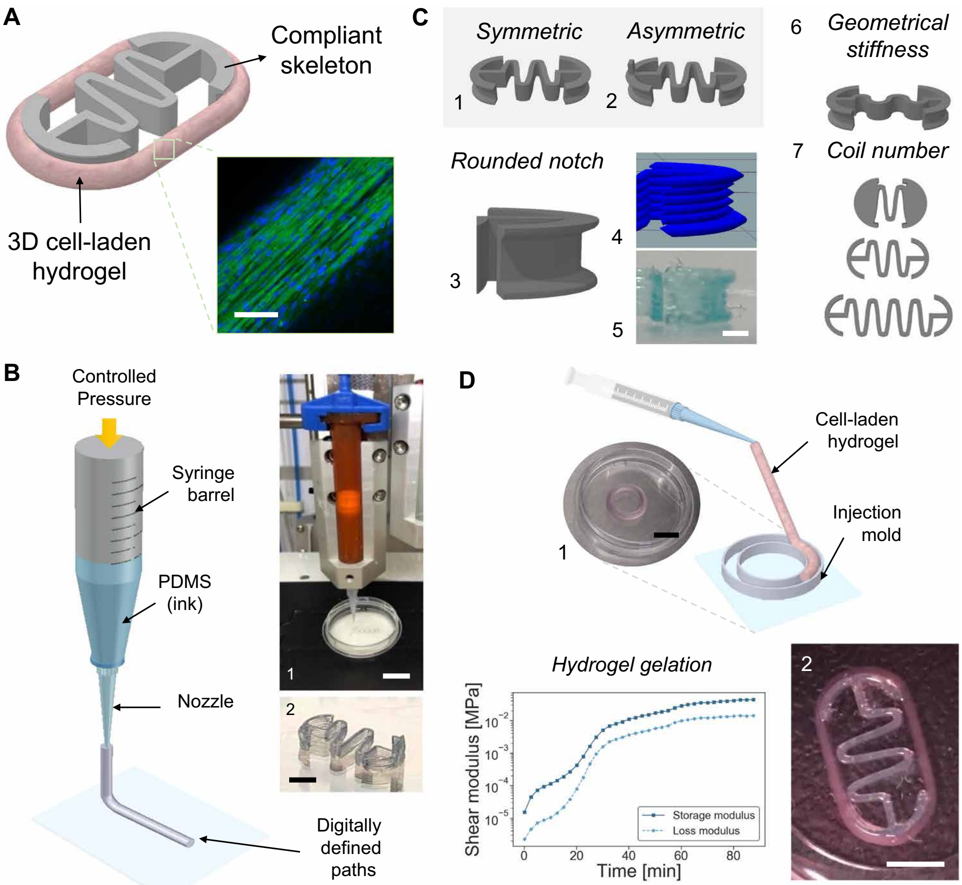

Fig. 2. Biobot design and fabrication. (**A**) Schematic of a biobot consisting of a skeletal muscle cell–laden hydrogel acting as a bio-actuator (inset: confocal laser scanning microscopy image of aligned skeletal muscle cells) assembled to a compliant spring-like PDMS skeleton. Scale bar, 100 μm. (**B**) 3D-printing process based on direct ink writing, where the hydrogel (PDMS) is printed onto a flat surface (1) to obtain the biobot compliant skeleton [image in (2)]. Scale bar, 1 cm in (1) and 3 mm in (2). (**C**) Different designs of the compliant skeleton, based on a (1) symmetric or (2) asymmetric serpentine flexure with a (3) rounded notch for a perfect assembly of the cell-laden hydrogel [the (4) 3D visualization of layer-by-layer view of the G-code instructions and (5) image of a printed notch]. The effect of (6) different angles on the geometrical stiffness and (7) coil numbers were explored to modulate the mechanical properties of the compliant skeleton design. Scale bar, 1 mm. (**D**) The fabrication process of 3D cell-laden molds [image of a mold (1)] and characterization of (2) mechanical properties related to the cell-laden hydrogel cross-linking, as well as a real image of a self-assembled biobot. Scale bar, 3 mm.

presented slightly similar values. Further experiments with 3D-printed skeletons revealed that case 3 was easily compressible and collapsed, making the serpentine coils touch and stick to each other. Therefore, the design of case 2 provided the appropriate stiffness conditions for muscle-induced compression in the expected force ranges. However, the compliant structure stiffness can also be tuned by changing the ratio of elastomer to curing agent (Fig. 4B). We explored the impact of the PDMS chemical composition by preparing skeletons with case 2 at different ratios of elastomer to curing agent: 1:20 (red), 1:15 (green), and 1:10 (blue), ordered from less to more stiffness. As expected, the compaction of the cell-laden hydrogel around a skeleton at 1:20 is higher than that at 1:10, demonstrating the feasibility to tune the structural configuration of the biobot's skeleton by changing its mechanical stiffness.

Having defined optimal serpentine structure, the asymmetry of the biohybrid robot was also studied by FEA simulations (Fig. 4C). Likewise, by simulating two uniaxial equivalent contraction profiles at both sides of the skeleton, we observed that the presence of a small post bulging out of one of the sides induced a differential compression of the structure. In this compression versus force plot, it can be seen how the maximum compression of the stiffer side (with the induced asymmetry), termed Δx_1, was larger than the compression in the softer side, Δx_2, as demonstrated on the geometrical stiffness evaluation. Last, we studied the feasibility of the buckling behavior by inducing a uniaxial compression force at both sides of the skeleton, but out of center, as indicated by the force vectors in Fig. 4D. These forces mimicked the passive compaction of the tissue that occurs during myogenesis (*35*, *43*). We hypothesize that this effect could be caused by a spontaneous symmetry breaking during tissue compaction, probably due to a combination of the heterogeneity of the muscle constructs that could lead to an asymmetric distribution of the compression forces and the interaction with close interfaces. For robotic systems at small scales, symmetry breaking is key to achieve efficient motion (*55*). Therefore, we expect that this differential compression produces a difference in the fluid flow fields, leading to directional motion.

It is known that dynamic mechanical stimulation is beneficial for the differentiation and maturation of skeletal muscle cells, because it mimics the conditions of native tissue (*56*, *57*). Therefore, we hypothesized that the spring-like configuration of the serpentine skeleton provided dynamic stimulation after spontaneous contractions by reacting with an opposite restoring force that could further expand the tissue, offering mechanical stretching in the form of a feedback loop. To demonstrate this, we compared two types of biobots: (i) the compliant and untethered spring-like skeleton and (ii) a two-post system that was tethered and less compliant (Fig. 5A). During myogenesis, we checked for the presence of spontaneous contractions via optical microscopy, revealing that, after 4 days (D4) of differentiation, only spring-like biobots were showing strong spontaneous contractions, fully synchronized and at a frequency of about 3 Hz, whereas bio-actuators in the two-post system were not showing any spontaneous contractions (Fig. 5B). At D8 of differentiation, the muscle tissue in the two-post system showed small, localized contractions that were not synchronized, and eventually, at D10, the spontaneous contractions were strong and globally distributed, as in the biohybrid robot (Fig. 5B and movie S1).

The movement index of the contractions, defined as the pixel difference between images in a small region of interest (ROI) of the

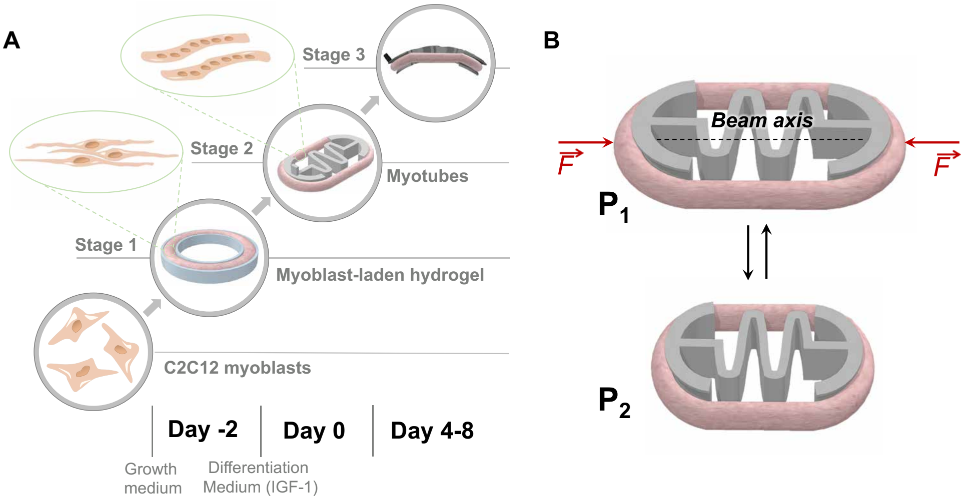

Fig. 3. Cell differentiation and compliant mechanism at the biobot platform. (**A**) Conceptual schematic of the cell maturation process at the biobot platform, along with the timeline in which C2C12 myoblast seeding, mold preparation (stage 1), assembly (stage 2), and bending (stage 3) take place. (**B**) Schematic representation of the compliant mechanism of the biobot, where compression (P_2) and expansion state (P_1) of the serpentine flexure are induced by the contraction forces of the muscle and spring-like relaxation behavior of the assembled muscle cell–based bio-actuator upon electric pulse stimulation.

tissue, is shown in fig. S1A at D4 of differentiation. It can be seen that only the biobot in a spring-like skeleton showed periodic spikes in its movement index (representing the spontaneous contractions), whereas the signal of the two-post system was mainly noise. A fast Fourier transform (FFT) of this signal (fig. S1B) further confirmed that only the former showed synchronized and defined contractions at 3 Hz, whereas the signal of the latter did not have any defined frequencies and was just noise.

The alignment of the myotubes within the tissue constructs was studied by directionality analysis using FFT of immunostaining images (Fig. 5C and fig. S2). In the spring-like skeleton, myotubes were highly aligned, and nuclei also showed elongation toward the same direction. However, in the two-post system, this alignment was not so outstanding. We hypothesize that the dynamic and compliant nature of the spring-like skeleton induces the alignment of the myotubes due to the constant stretching supplied by spontaneous contractions and restoring force. The strength of the contractions was also evaluated and compared (Fig. 5D and movie S2). Although the bio-actuator in the two-post system did not present spontaneous contractions at D4, EPS could induce contractions in the tissue, which were of a similar magnitude to those induced in the biobot. However, force measurements after several days in differentiation demonstrated that the muscle tissue of the spring-like biobot had increased its force almost fourfold, whereas the two-post bio-actuator only by twofold, which could be related to the improved alignment of the cells in the spring-like skeleton (Fig. 5D). Confocal immunostaining of myosin heavy chain II (MyHCII) and cell nuclei showed the presence of sarcomeric structures in the hybrid biobot (Fig. 5E).

Further biological characterizations were performed to elucidate the reason behind the force difference between tissues in the two-post or the spring-like system. The diameter of myotubes differentiated in both systems was compared and yielded values between 13 and 14 μm without statistically significant differences between them, similar to previous reports in the literature (*21*, *58*); therefore, the force difference could not be due to hypertrophic myotubes (fig. S3). Viability/metabolic activity assays showed a plateau after D2 of differentiation (as the cells were not proliferating anymore); thus, the tissues in the two-post or spring-like systems were equally viable (Fig. 5F). Last, real-time quantitative polymerase chain reaction (RT-qPCR) of several maturation-related genes (myogenin, MyHCI, MyHCIIa, MyHCIIb, and MyHCIIx) was performed at different time points (D0, D4, and D8) for both systems (notice that D0 coincides, because both samples were transferred to their scaffolds at that point). In general, we observed a down-regulation of MyHCI and up-regulation of the isoforms of MyHCII, as expected for skeletal muscle tissue during maturation, in a slow-to-fast myosin transition (*59*, *60*). Although not statistically significant because of the high variability of the samples, MyHCIIa in average seemed to be up-regulated in the spring-like skeleton compared with the two-post system, which could be related to the stronger force output reported in Fig. 5D. In any case, given the same levels of myotube diameter, similar metabolic activity, and comparable expression of myosin genes, the increased force generation of the spring-like biobots is likely to have its strongest contribution from the enhanced alignment and the restoring force feedback.

After at least D4 of differentiation, the hybrid biobots could show a spontaneous symmetry breaking leading to a buckling structure, as depicted in Fig. 3A and validated in Fig. 4D. However, due to the hydrophobicity of PDMS and surface tension at the air-liquid interface, biobots with a symmetric skeleton remained floating without showing any buckling behavior (Fig. 6A1 and movie S3). An asymmetry in the form of buckling was induced in the symmetrical skeletons by forcing the biobot inside the culture medium, while working in a plastic petri dish, during the differentiation process. The presence of a notch at each skeleton's edge prevents the release of the cell-laden hydrogel when the bending of the biohybrid robot takes place. Although the glass surface aids a better assembly of the cell-laden hydrogel to the notch at the early maturation stages (from D0 to D5) by ensuring that the PDMS skeleton remains completely flat due to the hydrophobic interactions, the plastic surface presents a different surface tension with a weaker interaction, allowing the desired buckling effect and efficient swimming motion.

For the biobots with a symmetric skeleton, two different cases were studied. In the first one, considered the biobot, maintained at the air-liquid interface, no substantial motion was observed (Fig. 6A1 and movie S3). However, when the symmetric biobot was placed near to the bottom surface, buckling deformation was spontaneously generated due to the heterogeneity of the muscle construct yielding a net compaction force outside its axis of symmetry (Fig. 6, A2 and A3), observing motion for some of the symmetric biobot upon EPS. This spontaneous symmetry breaking and thus the degree of deformation could not be controlled, but it was dependent on the

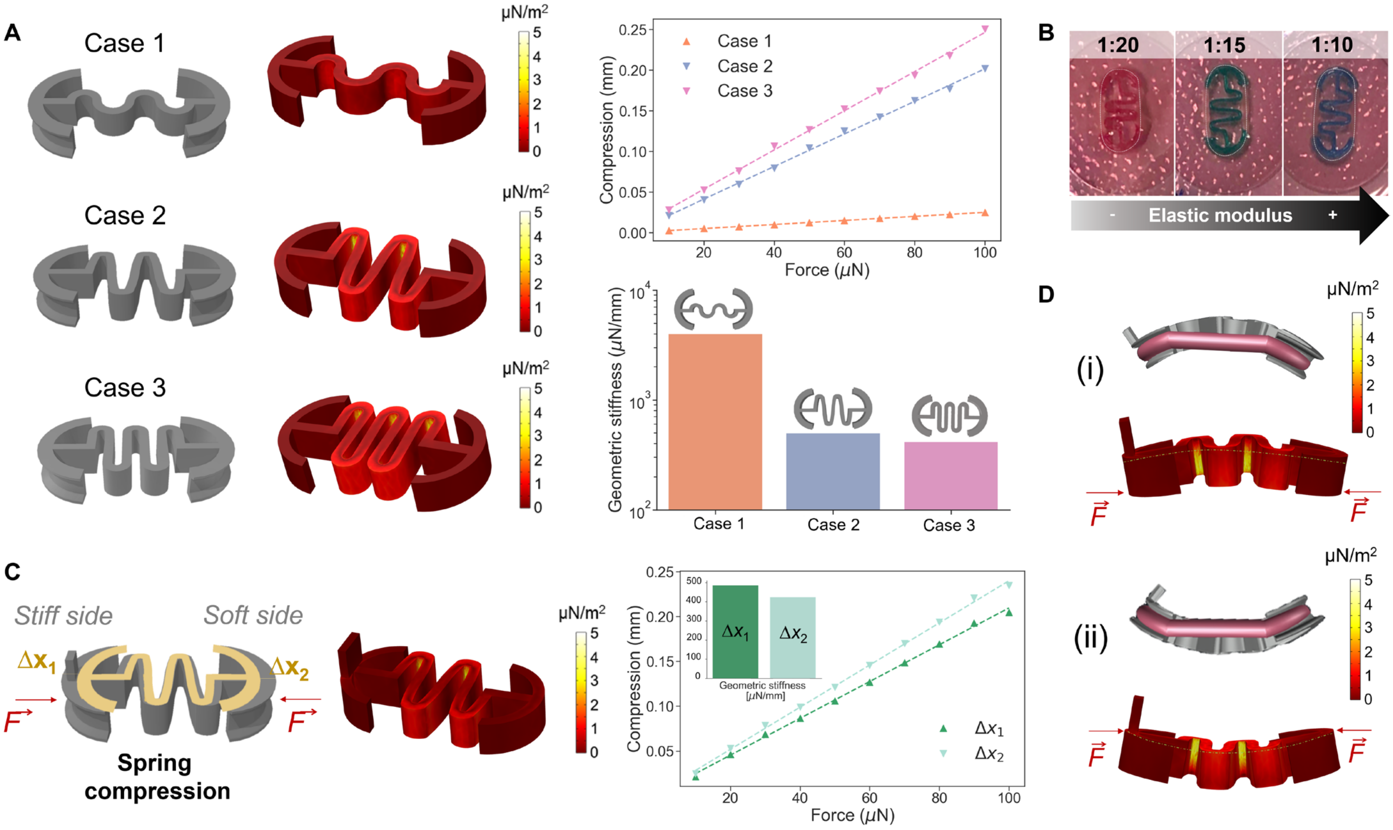

Fig. 4. FEA simulations of mechanical deformation on biobot compliant skeleton. (**A**) Three different cases were considered to optimize the coil curvature and shape, depending on the geometrical stiffness of the construct. Next to the 3D representation of each case, the von Mises stresses of each structure after a symmetrical load of 100 μN on each side are presented. The maximum compression of the skeleton in terms of the applied force (right top) and geometrical stiffness (right bottom) was obtained per each of the three cases. (**B**) Stiffness modulation properties tuned by PDMS chemical composition; different colored dyes were included to the PDMS to differentiate them, corresponding red, green, and blue to 1:20, 1:15, and 1:10, respectively. (**C**) Stiffness evaluation in presence of an asymmetric skeleton. (**D**) Bending analysis for studying the buckling behavior on the compliant skeleton, revealing that there is inhomogeneity in the compaction that can be related to buckling, which can happen both toward the leg and the opposite direction.

stiffness of the material, given by the curing agent–to–base ratio of PDMS. In Fig. 6B, we can see that low-stiffness PDMS (left) would completely compress and collapse the structure, whereas higher stiffnesses (middle and right) would allow some freedom of movement that could result in net motion. Figure 6C shows an example of the displacement of the best-case scenario of symmetric swimming, which could reach maximum speeds of 100 to 200 μm/s (or 0.5 to 1 body length/min), increasing with frequency (movie S4). This type of motion could resemble the swimming style of certain fish near surfaces, such as the burst-and-coast behavior of zebrafishes, characterized by sporadic bursts followed by coasting phases (*61*, *62*). The strong hydrodynamic couplings between the flow field around the biobots and the bottom surface, which are known to play a substantial role in the motion of microorganisms (*63*), may also play a substantial part in this case. For instance, it is known that hydrodynamic coupling induces the alignment of the swimming direction of a microorganism with the nearby surface (*63*–*66*). It should be considered, however, that the motion resulting from symmetric skeletons was not predictable, because it strongly depended on the degree of buckling curvature, which could not be controlled. Moreover, both the speed and the direction of motion were not clearly defined, because they relied on spontaneous symmetry breaking of the structure and its interactions with the surfaces. Therefore, consistent and controllable motion was only obtained when an asymmetry was previously incorporated in the design.

Motion with asymmetric skeletons proved to be predictable in terms of yield and direction of swimming. The presence of the post on one of the sides of the skeleton's design induced a different stiffness of the two sides of the skeletons, as previously demonstrated by FEA analysis in Fig. 4C, as well as allowing stable floating of the buckled structure, unlike in the case of the symmetric biobots that required to be placed to the bottom surface (Fig. 7A). In general, whereas symmetric designs moved only under certain conditions that broke their symmetry at speeds lower than 100 μm/s, asymmetric biobots swam at higher speeds and in a consistent manner (direction opposite to the post) although with great variability between samples (Fig. 7B). Moreover, the yield of biobots (defined as the percentage of biobots moving with respect to the full sample) was much higher for asymmetric skeletons (~60%) than for symmetric ones (~25%).

Three tracking examples for the biobots with an asymmetric skeleton at different stimulation frequencies are also shown, where speeds of more than 700 to 800 μm/s for frequencies of 2 and 10 Hz and 550 μm/s for 1 Hz can be observed (Fig. 7C and movie S5). In

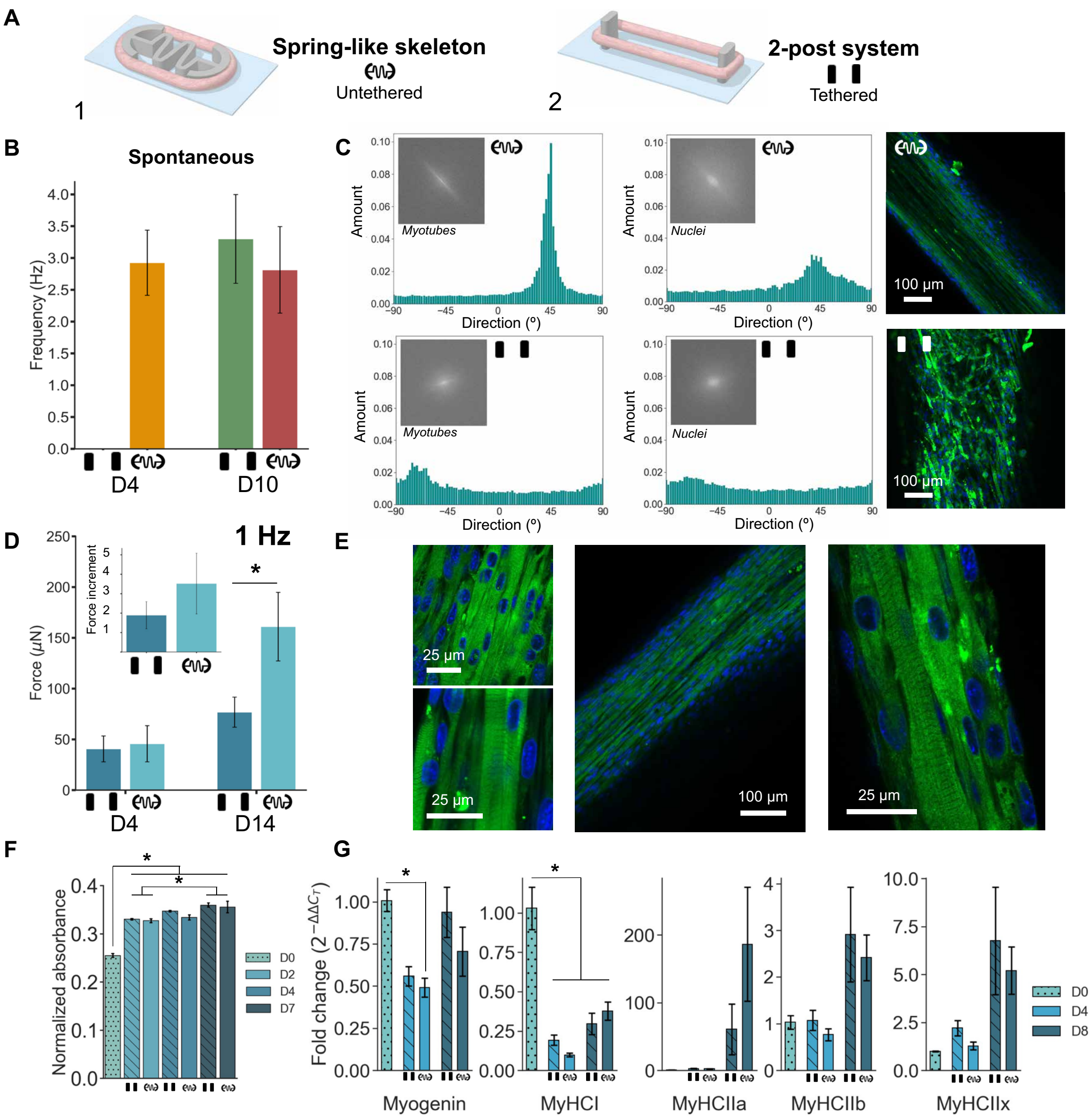

Fig. 5. Force generation and biological characterization of skeletal muscle biobots. (**A**) Schematic of spring-like skeleton setup (1) and two-post system (2). (**B**) Spontaneous contraction evaluation at D4 and D10. $N = 4$ to 6. (**C**) Directionality histograms for the myotubes and nuclei structures when matured in the two-post system and the spring skeleton. (**D**) Force measurements of the two-post system and biobot system at D4 and D14 of differentiation and force increment (inset). $N = 3$ to 4. Asterisk indicates significant difference ($P < 0.05$; Student's t test). (**E**) Confocal evaluation of the tissue ring in a biobot showing the presence of sarcomeric structures. MyHCII, green; cell nuclei, blue. (**F**) PrestoBlue viability/metabolic activity assay showing the normalized absorbance for samples at D0 of differentiation in the mold (dotted bar) and differentiated in the two-post (stripped) or spring-like (empty) systems. $N = 3$ to 4. Asterisk indicates significant difference ($P < 0.05$; Tukey's post hoc test). (**G**) RT-qPCR analysis for samples at D0 in the mold (dotted bar) and differentiated into the two-post (stripped) or spring-like (empty) systems. $N = 3$. Asterisk indicates significant difference ($P < 0.05$; Tukey's post hoc test). Error bars in all figures represent SEM.

the insets of 1 and 2 Hz, we can see how the motion occurs in a stepwise manner, whereas for 5 Hz, it is more continuous. Comparing the average trajectories of both designs from all the trackings, we found that both symmetric and asymmetric biobots were able to achieve motion. An interesting common feature of asymmetric biobots is the stepwise motion, consistent with swimming mechanism driven by inertia (Fig. 7D). In fluid mechanics, the relationship between inertial forces and viscous forces during the motion of a swimmer is known as the Reynolds number (*Re*). This dimensionless quantity allows differentiation between regimes of motion in which laminar flows (typical of viscous motion) or turbulent flows (typical of inertial motion) are dominant. At low *Re* (≪1), where viscous forces dominate, the fluid dynamics are described by the time-independent Stokes equation, in which inertial components are considered negligible. At this scale, the "scallop theorem" by Purcell dictates that a swimmer must perform nonreciprocal or time-irreversible motion to achieve a net displacement different from zero (*67*). Microorganisms manage to break this time-reversal symmetry by rotatory motions

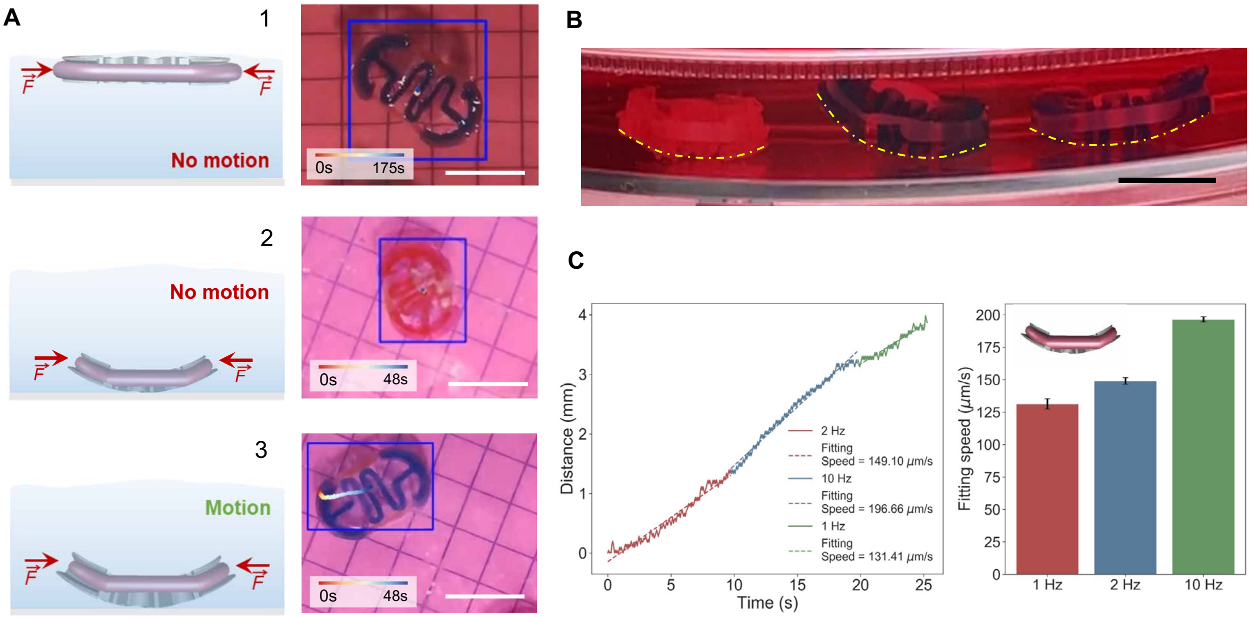

Fig. 6. Symmetric biobot motion evaluation. (**A**) Schematic of the side position and top image (photograph) from the symmetric biobot when located at the interface (1) and in solution for the two cases where no motion (2) and motion (3) is taking place. Scale bars, 10 mm. (**B**) Side image of three different biobots with different stiffnesses, with the corresponding bending due to the buckling effect indicated in a dashed yellow line. Scale bar, 10 mm. (**C**) Speed analysis for the case of the symmetric biobot at different frequencies. Error bars represent the error of the least-squares fitting.

(*68*), like those of bacterial flagella (*69*), which have been mimicked by artificial micropropellers (*70*) or biohybrid swimmers based on cardiac cells (*71*). In our case, the compression mechanism of the skeletal muscle tissue against the skeleton is time-reversible because the shape changes are identical if time is reversed. This bioswimmer, therefore, should not present motion at low *Re*. The *Re* number is defined as $Re = {}^{vL}/_{\nu}$ where v is the characteristic fluid velocity, L the characteristic length of the swimmer, and ν the kinematic viscosity of the fluid. In our case, given an approximated size of 10 cm and speeds of the biobots between 100 and 500 μm/s, we find *Re* numbers of the order of 1 to 5. In this range, both viscosity and inertia play a substantial role, and the motion cannot be considered neither purely viscous nor purely inertial.

Hydrodynamic simulations were performed to demonstrate that the fluid inertia and the asymmetric deformation of the biobot upon muscle contraction are key to its locomotion. Because of the high computational power of simulating the deformation of 3D structures coupled with hydrodynamics, a 2D model was used instead (see the Supplementary Materials). As shown schematically in Fig. 8A, we modeled the time-dependent deformation of the left side of the biobot as $d_l(t) = \Delta_l\, g(t)$ and of its right side as $d_r(t) = \Delta_r\, g(t)$. The deformation of the skeleton in the middle was set to vary linearly between these two values (see the Supplementary Materials). The maximum compressions Δ_l and Δ_r were equal in the case of a symmetric biobot but different in the case of an asymmetric one with distinct geometric stiffness on each side. The periodic deformation of the skeleton due to the contraction and the relaxation of the muscle cells $g(t)$ was chosen to closely follow the measured deformation in the experiments, as shown in Fig. 8B. This contraction profile is typical of skeletal muscle tissue, because it is known to go through a fast period of contraction followed by a slower relaxation (Fig. 7D) (*43*). Because the contraction and relaxation of the skeleton are time-reversible, we expected propulsion only if Δ_l is different from Δ_r. The snapshots in Fig. 8C show the magnitude of the velocity field and the streamlines around the biobot during one contraction/relaxation period as computed from the numerical simulations. In the top panels, displaying the symmetric case, the left and the right side of the biobot deformed in the same way, $\Delta_r = \Delta_l$. As a result, the streamlines on the left and on the right of the biobot were highly symmetric, and the net displacement of the biobot, averaged over one period, was negligible. This is confirmed by looking at Fig. 8 (D and E), which shows the velocity of the symmetric biobot as a function of time and its average over one period.

In contrast, a biobot with a stiffer right side deformed asymmetrically, undergoing a larger deformation along its left side $\Delta_l > \Delta_r$. In the bottom panels of Fig. 8C, we show snapshots of the magnitude of the velocity and of the streamlines during one period for an asymmetric biobot. The streamlines at $t = 0.5$ s and $t = 0.75$ s indicate that the biobot is moving from the right to the left (right side of the skeleton corresponding to the stiffer side), which is in agreement with that observed in the experiments. This finding is confirmed in Fig. 8D where the velocity of an asymmetric biobot is shown to be negative, i.e., from the right to the left, during the entire period. The average speed of the asymmetric biobot over one period is compared with that of the symmetric one in Fig. 8E, confirming our hypothesis that an asymmetric deformation of the biobot is necessary for its locomotion.

DISCUSSION

Biological robots based on skeletal muscle tissue are of interest to the field of soft robotics because of the inherent properties of natural tissue that are difficult to replicate with artificial actuators. Muscle-based biobots have been proposed as tissue models to study

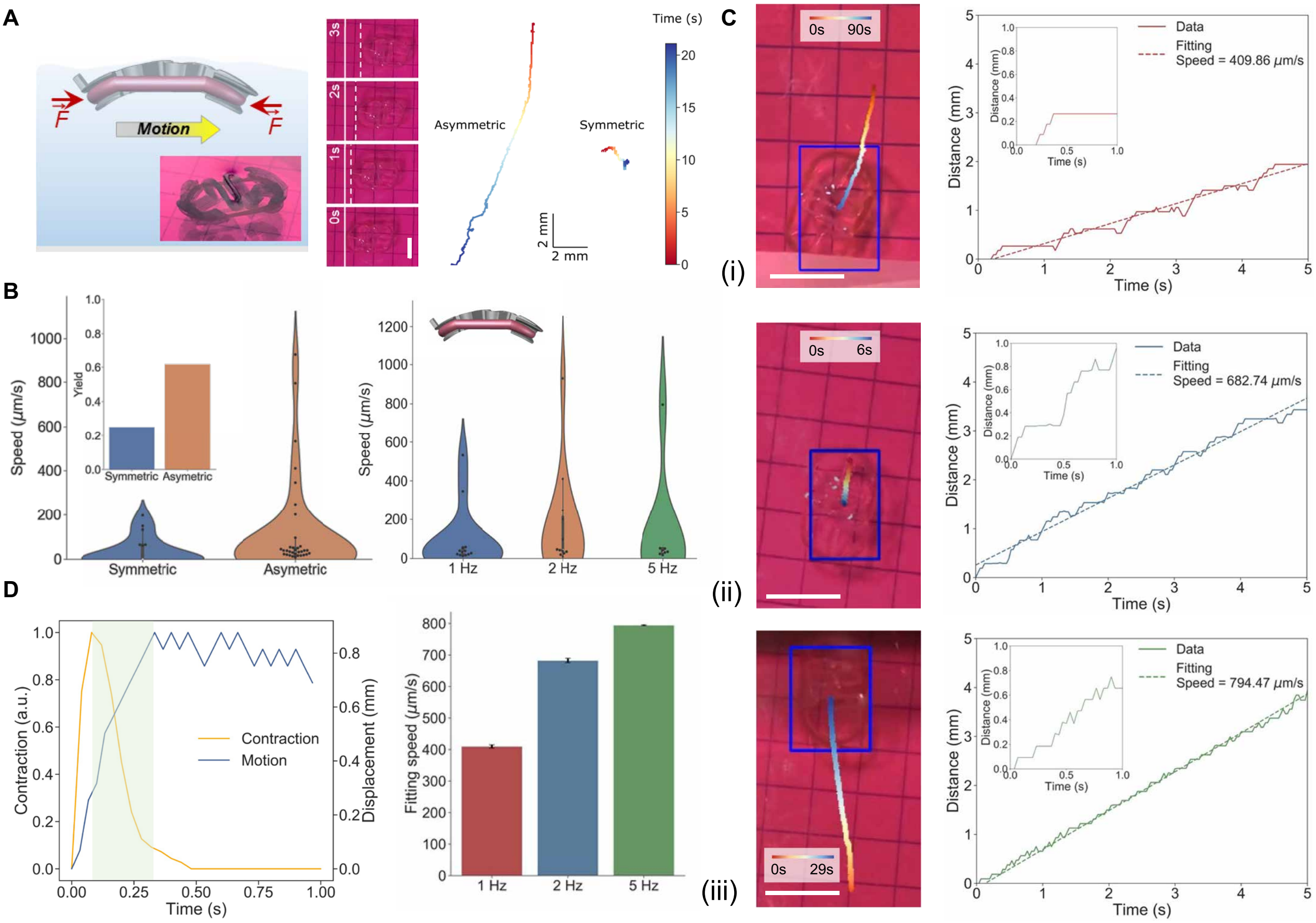

Fig. 7. Asymmetric biobot evaluation. (**A**) Schematic of the side position and time step image of an asymmetric biobot motion for 3 s and its corresponding speed under different EPS frequencies. On the right, sample trajectories of an asymmetric and symmetric biobot. (**B**) Violin plots of the speed of symmetric versus asymmetric biobots. Yield of moving biobots with respect to the total sample (inset). On the right, violin plots of the speed of asymmetric biobots for different frequencies. (**C**) Motion evaluation of the asymmetric biobot, depicting its motion efficiency with an image where the corresponding track is shown, as well as its displacement over time, at (i) 1 Hz, (ii) 2 Hz, and (iii) 5 Hz. Scale bars, 10 mm. (**D**) Left: Superposition of a measured contraction (yellow) with the displacement of a biobot after one contraction. The green shadowed portion represents the region of motion that can only be explained by inertia. Right: Average motion of asymmetric biobots upon different EPS frequencies. Error bars represent the error of the least-squares fitting. a.u., arbitrary units.

muscle development and regeneration (*43*, *72*) or as drug-testing platforms in the biomedical field (*73*, *74*), but these actuators are also posed as excellent candidates to study the integration of tissue with complex artificial materials to understand or improve motion mechanisms through biomimetic approaches in robotic platforms (*30*, *31*, *34*, *35*). We have shown that a biohybrid robot based on skeletal muscle cells can swim at speeds comparable to those of their cardiac counterparts (Fig. 1) and also take advantage of the adaptability and control capabilities inherent to skeletal muscle cells. We reported a biological robot based on a flexible serpentine spring design that is optimized through simulations and subsequently 3D-printed. The advantage of a compliant spring-like scaffold, instead of a stiffer or tethered one, lies in the improved differentiation of the tissue through mechanical self-stimulation upon spontaneous contractions, which creates a feedback loop due to the restoring force of the spring. Moreover, the asymmetry from the serpentine spring skeleton allows the structure to move with two different modes: by inertial swimming at the interface or coasting near a bottom surface. Serpentine spring structures are well known in the MEMS field to create flexible structures by working with microfabrication techniques (*75*, *76*). Although serpentine springs have been implemented in untethered micro–force sensing microrobots to obtain compliant structures (*77*), such structures have not been included before in a soft robotic living system. The design of the serpentine spring was printed using additive manufacturing, obtaining a compliant structure that may be of interest for the design of future 3D-printed robotic platforms.

The optimization of the designs, based on several features like asymmetry or coil curvature, was performed via FEA simulations, which allowed us to find the appropriate geometrical stiffnesses of each case and then experimentally test them. As expected, we found that the addition of an asymmetric feature in one of the sides resulted in a differential compression of the skeleton, which is known to be necessary for efficient motion (*35*). Moreover, force measurements revealed that differentiation in a compliant spring-like skeleton was beneficial when compared with other static tethered skeletons, such as a two-post system. The muscle tissue under these conditions showed earlier spontaneous contractions and greater increments of force during the differentiation process. We hypothesize that the dynamic compliance of the skeleton, reacting to the compression with a restoring force, provided an additional level of cyclic mechanical stimulation that helped to achieve a better degree of differentiation. The potential to expand the use of such skeleton in other muscle-based biobot configurations would represent an alternative approach to implement tailored training protocols that do not require for any external stimuli.

Last, we characterized the motion of two types of biohybrid robots: a symmetric swimmer and an asymmetric swimmer. For the former, we found that motion at the air-liquid interface was not possible because of the generated symmetric flow fields, which was supported by hydrodynamic simulations. In contrast, when the symmetric biobots were placed into the culture medium, a buckling behavior was observed, and the swimmer adopted a curved structure that allowed motion at low speeds, although such motion was unreliable, most likely due to interactions between the generated flow fields and the surface. Asymmetric biobots, however, presented a reliable and consistent motion, because they already displayed buckling when floating in the air-liquid interface. Stimulation with EPS revealed high speeds up to 800 μm/s, and motion studies and hydrodynamic simulations consistently confirmed the hypothesis that inertia plays a key role in the motion mechanism. Future work should aim at understanding the interactions between the skeleton and surfaces to comprehend the exact parameters governing this type of motion and cooperative behavior of several biobots. Moreover, the scalability of these biobots could be investigated by comparing the motion of swimmers with different numbers of coils and exploring other configurations, mainly because of the versatility that 3D bioprinting offers in terms of shape and multimaterial 3D printing, as well as studying the implementation of nanocomposites.

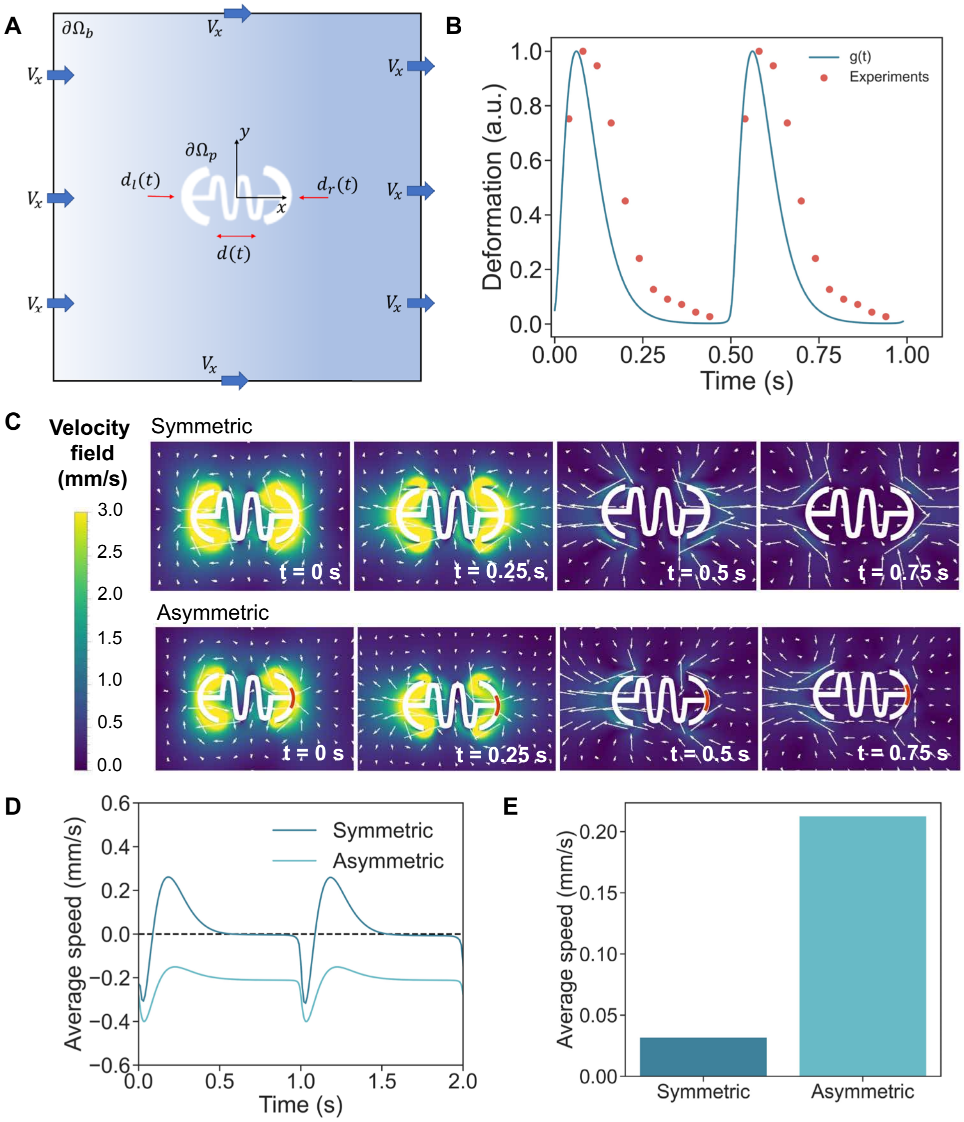

Fig. 8. Hydrodynamics of biobot locomotion. (**A**) Schematics of the 2D computational model. (**B**) Periodic deformation of the biobot used in the simulation compared with that measured in the experiments. (**C**) Magnitude of the velocity field and streamlines at four different instants during one period, in the case of a biobot driven at 1 Hz. Top: Results for a symmetric biobot. Bottom: Results for an asymmetric biobot. The orange icon at the right side of the biobot represents the region with the post (stiffer section experiencing smaller deformations). (**D**) Evolution of the *x* component of the velocity of the biobot during two periods. (**E**) Average speed of the biobot over one period in the case of a stimulation at 1 Hz.

In summary, the biohybrid swimmer based on skeletal muscle cells hereby reported moves at speeds faster than the largest skeletal muscle–based biobots up to date (*49*) and comparable with other cardiomyocyte-based bioswimmers (*30*). We used 3D printing of PDMS to fabricate serpentine-like skeletons that can act as a spring when a muscle ring compresses them, resulting in compliant scaffolds that aid in the differentiation of the tissue. The optimization of the designs via FEA simulations allowed us to find the appropriate geometrical stiffnesses by studying their asymmetry and coil curvature. We found that differentiation in a compliant spring-like skeleton was beneficial when compared with other static tethered skeletons because of its associated mechanical self-training capabilities, resulting in earlier spontaneous contractions and greater increments of force during the differentiation process. We hypothesize that the dynamic compliance of the skeleton, reacting to the compression with a restoring force, provides an additional level of cyclic mechanical stimulation that aids to achieve an improved maturation. In addition, the hydrodynamic study of the different motion modes provides a fundamental understanding over its motion mechanism, demonstrating the potential of applying this serpentine-like structure to provide asymmetry and achieve enhanced force outputs on future biobot configurations. Such biohybrid compliant actuators can be envisioned as basic units to construct a modular system that allows scaling up the current biohybrid robotic systems, not only providing better muscle cell alignment that affects the final force output but also obtaining additional degrees of freedom in terms of motion capabilities due to the observed buckling effect (i.e., agonistic-antagonist joint actuator). Further research in the biohybrid robotics field should be focused on the integration of several tissues and obtaining more complex, yet useful, ways of actuation that can finally prove the benefits of using native muscle tissue instead of artificial soft actuators. Once achieved, the next main challenges will reside in ensuring long-term stability of the constructs and tolerance to different environments and requiring the implementation of unconventional and soft bioreactors to protect the tissue and the improvement of the control mechanisms. All these advances will undoubtedly imply a coordinated interdisciplinary effort between different fields of expertise, ranging from 3D bioengineering and biology to materials science and mechanical engineering.

MATERIALS AND METHODS

Biobot fabrication

C2C12 mouse myoblasts were purchased from the American Type Culture Collection. GM consisted of high-glucose Dulbecco's modified Eagle's medium (DMEM; Gibco) supplemented with 10% fetal bovine serum, 200 nM L-glutamine, and 1% penicillin-streptomycin. Cells below passage 4 were used before reaching 80% confluency in Corning T-75 flasks. DM consisted of high-glucose DMEM containing 10% horse serum (Gibco), 200 nM L-glutamine (Gibco), 1% penicillin-streptomycin (Gibco), IGF-1 (50 ng/ml; Sigma-Aldrich), and ACA (1 mg/ml; Sigma-Aldrich). C2C12 skeletal myoblasts were harvested from the flask when reaching 80% confluency. The mixture adapted from Raman *et al.* (*42*) (see the Supplementary Materials) was manually casted immediately on a 3D-printed PDMS injection mold. The tissue construct was left in a cell incubator (37°C, 5% CO_2) for 30 min, the GM supplemented with ACA to avoid degradation of collagen by proteases was added, and the tissue construct was kept for 2 days. Then, the tissue was gently lifted from the mold and transferred to either (i) a 3D-printed compliant skeleton or (ii) a two-post system. Spring-like skeletons of different ratios (1:20, 1:15, or 1:10, with or without dye) were cured at 80°C overnight (*78*). The designs of the skeletons were done with AutoCAD (v.2019), exported as .stl files, and transformed into GCode, to be later printed with Cellink's Inkredible+ 3D bioprinter. The two-post system (3 mm high, 0.5 mm wide, and with 2 mm of lateral width) was 3D-printed with PDMS of a 1:20 ratio and cross-linked at 37°C for several days. Once the cell-laden scaffold was transferred to the compliant skeleton, the culture medium was changed to DM supplemented with ACA and IGF-1. After 4 days in DM, the structure was drawn in a plastic petri dish to obtain the desired buckling effect.

Biobot force characterization

The protocol described by Mestre *et al.* (*43*) for force measurements in a two-post system for muscle-based actuators was adapted to determine the role of the compliant skeleton on the fabricated biobots' final force. The recording of the whole setup undergoing EPS was carried out inside an inverted microscope (DMi8, Leica), in a chamber that mimicked physiological conditions (37°C and 5% CO_2). For force measurement of the biobots in Fig. 6, the tissue was gently transferred at D4 or D14, depending on the experiment, into a two-post system, and their force was measured by deflection of the posts by the cell-laden scaffold. Pulses of different frequencies of 1 ms were applied, keeping a constant voltage of 15 V. Euler-Bernoulli's beam bending equation was used to estimate the forces and stresses exerted against the posts to the tissue during electrical stimulation (*43*) (more details in the Supplementary Materials).

Motion analysis

Motion evaluation of the biohybrid robot was performed with a homemade Python tracking script based on computer vision algorithms that could characterize the motion of the biobots after being recorded with any type of smartphone camera (Fig. 6). In brief, the video file of the recorded biobots was loaded into the script, and the first frame was prompted for the user to manually select an ROI covering the whole biobot area (fig. S5). Then, an object-tracking algorithm based on an online AdaBoost feature selection (*79*) was applied to this ROI through every frame of the video (more details in the Supplementary Materials).

Statistical analysis

Experiments from spontaneous contractions and force measurement in Fig. 5D were performed for $N = 3$ to 6 independent repeats, and error bars represent SEM. Statistical significance is indicated by $*P < 0.05$ (Student's *t* test). Normality was assessed with the Shapiro-Wilk test and equality of variances with the Levene's test. Viability/metabolic activity assays in Fig. 5F and RT-qPCR in Fig. 5G were performed for $N = 3$ to 4 and $N = 3$ independent repeats, respectively, and error bars represent SEM. Statistical significance is indicated by $*P < 0.05$ (Tukey's post hoc test for multiple comparisons). Before Tukey's post hoc test, one-way analysis of variance (ANOVA) was performed, and the normality of the model residuals assessed with the Shapiro-Wilk test and equality of variances with the Levene's test. Motion fittings in Figs. 6C and 7D were performed with the least-squares fitting method to a linear equation of the form $x = v \cdot t$, from which the speed was extracted. In these plots, the error bars correspond to the error of the fitting. Violin plots and motion yield values of Fig. 7B come from $N = 26$ asymmetric and $N = 15$ symmetric biobots. Data in tabulated form and a more thorough description of the statistical analysis are available in the Supplementary Materials.

SUPPLEMENTARY MATERIALS

robotics.sciencemag.org/cgi/content/full/6/53/eabe7577/DC1
Materials and Methods
Data from all figures
Fig. S1. Movement index from the spontaneous contraction evaluation.
Fig. S2. Immunostaining studies by confocal microscopy.
Fig. S3. Myotube diameter study.
Fig. S4. EPS setup.
Fig. S5. Home-made script for tracking of biobots.
Movie S1. Spontaneous contraction evaluation.
Movie S2. Force evaluation between the two-post system and the spring-like biobot.
Movie S3. Spring-like symmetric biobot actuated at the air-liquid interface (control).
Movie S4. Spring-like symmetric biobot at the bottom surface actuated at different frequencies.
Movie S5. Spring-like asymmetric biobot at the air-liquid interface actuated at different frequencies.

REFERENCES AND NOTES

1. S. Camazine, J. L. Deneubourg, N. R. Franks, J. Sneyd, E. Bonabeau, G. Theraula, *Self-Organization in Biological Systems* (Princeton Studies in Complexity, Princeton Univ. Press, 2003).
2. P. Egan, R. Sinko, P. R. Leduc, S. Keten, The role of mechanics in biological and bio-inspired systems. *Nat. Commun.* **6**, 7418 (2015).
3. G. Li, Self-healing in biological systems, In *Self-Healing Composites*, G. Li (Ed.) (John Wiley & Sons Ltd, 2014), pp. 21–34.
4. D. B. Dusenbery, Spatial sensing of stimulus gradients can be superior to temporal sensing for free-swimming bacteria. *Biophys. J.* **74**, 2272–2277 (1998).
5. L. Ricotti, A. Menciassi, Bio-hybrid muscle cell-based actuators. *Biomed. Microdevices* **14**, 987–998 (2012).
6. T. Patino, R. Mestre, S. Sánchez, Miniaturized soft bio-hybrid robotics: A step forward into healthcare applications. *Lab Chip* **16**, 3626–3630 (2016).
7. M. Cianchetti, C. Laschi, A. Menciassi, P. Dario, Biomedical applications of soft robotics. *Nat. Rev. Mater.* **3**, 143–153 (2018).
8. L. Ricotti, B. Trimmer, A. W. Feinberg, R. Raman, K. K. Parker, R. Bashir, M. Sitti, S. Martel, P. Dario, A. Menciassi, Biohybrid actuators for robotics: A review of devices actuated by living cells. *Sci. Robot.* **2**, eaaq0495 (2017).
9. M. Wehner, R. L. Truby, D. J. Fitzgerald, B. Mosadegh, G. M. Whitesides, J. A. Lewis, R. J. Wood, An integrated design and fabrication strategy for entirely soft, autonomous robots. *Nature* **536**, 451–455 (2016).
10. R. F. Shepherd, F. Ilievski, W. Choi, S. A. Morin, A. A. Stokes, A. D. Mazzeo, X. Chen, M. Wang, G. M. Whitesides, Multigait soft robot. *Proc. Natl. Acad. Sci.* **108**, 20400–20403 (2011).
11. M. T. Tolley, R. F. Shepherd, B. Mosadegh, K. C. Galloway, M. Wehner, M. Karpelson, R. J. Wood, G. M. Whitesides, A resilient, untethered soft robot. *Soft Robot.* **1**, 213–223 (2014).
12. R. V. Martinez, J. L. Branch, C. R. Fish, L. Jin, R. F. Shepherd, R. M. D. Nunes, Z. Suo, G. M. Whitesides, Robotic tentacles with three-dimensional mobility based on flexible elastomers. *Adv. Mater.* **25**, 205–212 (2013).
13. G. K. Klute, J. M. Czerniecki, B. Hannaford, Artificial muscles: Actuators for biorobotic systems. *Int. J. Robot. Res.* **21**, 295–309 (2002).
14. R. H. Baughman, Playing nature's game with artificial muscles. *Science* **308**, 63–65 (2005).
15. C. Appiah, C. Arndt, K. Siemsen, A. Heitmann, A. Staubitz, C. Selhuber-Unkel, Living materials herald a new era in soft robotics. *Adv. Mater.* **31**, 1807747 (2019).
16. L. Sun, Y. Yu, Z. Chen, F. Bian, F. Ye, L. Sun, Y. Zhao, Biohybrid robotics with living cell actuation. *Chem. Soc. Rev.* **49**, 4043–4069 (2020).
17. J. Xi, J. J. Schmidt, C. D. Montemagno, Self-assembled microdevices driven by muscle. *Nat. Mater.* **4**, 180–184 (2005).
18. A. W. Feinberg, A. Feigel, S. S. Shevkoplyas, S. Sheehy, G. M. Whitesides, K. K. Parker, Muscular thin films for building actuators and powering devices. *Science* **317**, 1366–1370 (2007).
19. J. Kim, J. Park, S. Yang, J. Baek, B. Kim, S. H. Lee, E.-S. Yoon, K. Chun, S. Park, Establishment of a fabrication method for a long-term actuated hybrid cell robot. *Lab Chip* **7**, 1504–1508 (2007).
20. V. Chan, K. Park, M. B. Collens, H. Kong, T. A. Saif, R. Bashir, Development of miniaturized walking biological machines. *Sci. Rep.* **2**, 857 (2012).
21. V. Hosseini, S. Ahadian, S. Ostrovidov, G. Camci-Unal, S. Chen, H. Kaji, M. Ramalingam, A. Khademhosseini, Engineered contractile skeletal muscle tissue on a microgrooved methacrylated gelatin substrate. *Tissue Eng. Part A* **18**, 2453–2465 (2012).
22. S. R. Shin, C. Shin, A. Memic, S. Shadmehr, M. Miscuglio, H. Y. Jung, S. M. Jung, H. Bae, A. Khademhosseini, X. S. Tang, M. R. Dokmeci, Aligned carbon nanotube-based flexible gel substrates for engineering biohybrid tissue actuators. *Adv. Funct. Mater.* **25**, 4486–4495 (2015).
23. T. H. Kim, C. H. Kwon, C. Lee, J. An, T. T. T. Phuong, S. H. Park, M. D. Lima, R. H. Baughman, T. M. Kang, S. J. Kim, Bio-inspired hybrid carbon nanotube muscles. *Sci. Rep.* **6**, 26687 (2016).
24. L. Ricotti, T. Fujie, Thin polymeric films for building biohybrid microrobots. *Bioinspir. Biomim.* **12**, 021001 (2017).
25. B. Xu, X. Han, Y. Hu, Y. Luo, C.-H. Chen, Z. Chen, P. Shi, A remotely controlled transformable soft robot based on engineered cardiac tissue construct. *Small* **15**, 1900006 (2019).
26. A. Hasebe, Y. Suematsu, S. Takeoka, T. Mazzocchi, L. Vannozzi, L. Ricotti, T. Fujie, Biohybrid actuators based on skeletal muscle-powered microgrooved ultrathin films consisting of poly(styrene-*block*-butadiene-*block* -styrene). *ACS Biomater Sci. Eng.* **5**, 5734–5743 (2019).
27. L. Vannozzi, T. Mazzocchi, A. Hasebe, S. Takeoka, T. Fujie, L. Ricotti, A coupled FEM-SPH modeling technique to investigate the contractility of biohybrid thin films. *Adv. Biosyst.* **4**, 1900306 (2020).
28. R. Takemura, T. Hoshino, Y. Akiyama, K. Morishima, in *2010 International Symposium on Micro-NanoMechatronics and Human Science: From Micro and Nano Scale Systems to Robotics and Mechatronics Systems, MHS 2010, Micro-Nano GCOE 2010, Bio-Manipulation 2010* (IEEE, 2010), vol. 8588, pp. 485–490.
29. M. T. Holley, N. Nagarajan, C. Danielson, P. Zorlutuna, K. Park, Development and characterization of muscle-based actuators for self-stabilizing swimming biorobots. *Lab Chip* **16**, 3473–3484 (2016).
30. S.-J. Park, M. Gazzola, K. S. Park, S. Park, V. di Santo, E. L. Blevins, J. U. Lind, P. H. Campbell, S. Dauth, A. K. Capulli, F. S. Pasqualini, S. Ahn, A. Cho, H. Yuan, B. M. Maoz, R. Vijaykumar, J.-W. Choi, K. Deisseroth, G. v. Lauder, L. Mahadevan, K. K. Parker, Phototactic guidance of a tissue-engineered soft-robotic ray. *Science* **353**, 158–162 (2016).
31. J. C. Nawroth, H. Lee, A. W. Feinberg, C. M. Ripplinger, M. L. McCain, A. Grosberg, J. O. Dabiri, K. K. Parker, A tissue-engineered jellyfish with biomimetic propulsion. *Nat. Biotechnol.* **30**, 792–797 (2012).
32. T. J. Wallin, J. Pikul, R. F. Shepherd, 3D printing of soft robotic systems. *Nat. Rev. Mater.* **3**, 84–100 (2018).
33. N. di Marzio, D. Eglin, T. Serra, L. Moroni, Bio-fabrication: Convergence of 3D bioprinting and nano-biomaterials in tissue engineering and regenerative medicine. *Front. Bioeng. Biotechnol.* **8**, 326 (2020).
34. Y. Morimoto, H. Onoe, S. Takeuchi, Biohybrid robot powered by an antagonistic pair of skeletal muscle tissues. *Sci. Robot.* **3**, eaat4440 (2018).
35. C. Cvetkovic, R. Raman, V. Chan, B. J. Williams, M. Tolish, P. Bajaj, M. S. Sakar, H. H. Asada, M. T. A. Saif, R. Bashir, Three-dimensionally printed biological machines powered by skeletal muscle. *Proc. Natl. Acad. Sci. U.S.A.* **111**, 10125–10130 (2014).
36. M. S. Sakar, D. Neal, T. Boudou, M. A. Borochin, Y. Li, R. Weiss, R. D. Kamm, C. S. Chen, H. H. Asada, Formation and optogenetic control of engineered 3D skeletal muscle bioactuators. *Lab Chip* **12**, 4976–4985 (2012).
37. M. Das, K. Wilson, P. Molnar, J. J. Hickman, Differentiation of skeletal muscle and integration of myotubes with silicon microstructures using serum-free medium and a synthetic silane substrate. *Nat. Protoc.* **2**, 1795–1801 (2007).
38. K. Shimizu, H. Sasaki, H. Hida, H. Fujita, K. Obinata, M. Shikida, E. Nagamori, Assembly of skeletal muscle cells on a Si-MEMS device and their generative force measurement. *Biomed. Microdevices* **12**, 247–252 (2010).
39. T. Boudou, W. R. Legant, A. Mu, M. A. Borochin, N. Thavandiran, M. Radisic, P. W. Zandstra, J. A. Epstein, K. B. Margulies, C. S. Chen, A microfabricated platform to measure and manipulate the mechanics of engineered cardiac microtissues. *Tissue Eng. Part A* **18**, 910–919 (2012).
40. T. Hoshino, K. Morishima, Muscle-powered cantilever for microtweezers with an artificial micro skeleton and rat primary myotubes. *J. Biomech. Sci. Eng.* **5**, 245–251 (2010).
41. K. Kabumoto, T. Hoshino, Y. Akiyama, K. Morishima, Voluntary movement controlled by the surface EMG signal for tissue-engineered skeletal muscle on a gripping tool. *Tissue Eng. Part A* **19**, 1695–1703 (2013).
42. R. Raman, C. Cvetkovic, R. Bashir, A modular approach to the design, fabrication, and characterization of muscle-powered biological machines. *Nat. Protoc.* **12**, 519–533 (2017).
43. R. Mestre, T. Patiño, X. Barceló, S. Anand, A. Pérez-Jiménez, S. Sánchez, Force modulation and adaptability of 3D-bioprinted biological actuators based on skeletal muscle tissue. *Adv. Mater. Technol.* **4**, 1800631 (2018).
44. R. Raman, C. Cvetkovic, S. G. M. Uzel, R. J. Platt, P. Sengupta, R. D. Kamm, Optogenetic skeletal muscle-powered adaptive biological machines. *Proc. Natl. Acad. Sci. U.S.A.* **113**, 3497–3502 (2016).
45. R. Raman, R. Bashir, Biomimicry, biofabrication, and biohybrid systems: The emergence and evolution of biological design. *Adv. Healthc. Mater.* **6**, 1700496 (2017).
46. C. Cvetkovic, M. H. Rich, R. Raman, H. Kong, R. Bashir, A 3D-printed platform for modular neuromuscular motor units. *Microsyst. Nanoeng.* **3**, 17015 (2017).
47. C. Cvetkovic, M. C. Ferrall-Fairbanks, E. Ko, L. Grant, H. Kong, M. O. Platt, R. Bashir, Investigating the life expectancy and proteolytic degradation of engineered skeletal muscle biological machines. *Sci. Rep.* **7**, 3775 (2017).
48. L. Grant, R. Raman, C. Cvetkovic, M. C. Ferrall-Fairbanks, G. J. Pagan-Diaz, P. Hadley, E. Ko, M. O. Platt, R. Bashir, Long-term cryopreservation and revival of tissue-engineered skeletal muscle. *Tissue Eng. Part A* **25**, 1023–1036 (2019).
49. G. J. Pagan-Diaz, X. Zhang, L. Grant, Y. Kim, O. Aydin, C. Cvetkovic, E. Ko, E. Solomon, J. Hollis, H. Kong, T. Saif, M. Gazzola, R. Bashir, Simulation and fabrication of stronger, larger, and faster walking biohybrid machines. *Adv. Funct. Mater.* **28**, 1801145 (2018).
50. Y. Kim, G. Pagan-Diaz, L. Gapinske, Y. Kim, J. Suh, E. Solomon, J. F. Harris, S. Nam, R. Bashir, Integration of graphene electrodes with 3D skeletal muscle tissue models. *Adv. Healthc. Mater.* **9**, 1901137 (2020).
51. O. Aydin, A. P. Passaro, M. Elhebeary, G. J. Pagan-Diaz, A. Fan, S. Nuethong, R. Bashir, S. L. Stice, M. T. A. Saif, Development of 3D neuromuscular bioactuators. *APL Bioeng.* **4**, 016107 (2020).
52. C. D. Kaufman, S. C. Liu, C. Cvetkovic, C. A. Lee, G. Naseri Kouzehgarani, R. Gillette, R. Bashir, M. U. Gillette, Emergence of functional neuromuscular junctions in an engineered, multicellular spinal cord-muscle bioactuator. *APL Bioeng.* **4**, 026104 (2020).

53. O. Aydin, X. Zhang, S. Nuethong, G. J. Pagan-Diaz, R. Bashir, M. Gazzola, M. T. A. Saif, Neuromuscular actuation of biohybrid motile bots. *Proc. Natl. Acad. Sci.* **116**, 19841–19847 (2019).
54. S. Hinds, W. Bian, R. G. Dennis, N. Bursac, The role of extracellular matrix composition in structure and function of bioengineered skeletal muscle. *Biomaterials* **32**, 3575–3583 (2011).
55. S. Wu, Q. Ze, R. Zhang, N. Hu, Y. Cheng, F. Yang, R. Zhao, Symmetry-breaking actuation mechanism for soft robotics and active metamaterials. *ACS Appl. Mater. Interfaces* **11**, 41649–41658 (2019).
56. C. A. Powell, B. L. Smiley, J. Mills, H. H. Vandenburgh, Mechanical stimulation improves tissue-engineered human skeletal muscle. *Am. J. Physiol. Cell Physiol.* **283**, C1557–C1565 (2002).
57. D. G. Moon, G. Christ, J. D. Stitzel, A. Atala, J. J. Yoo, Cyclic mechanical preconditioning improves engineered muscle contraction. *Tissue Eng. Part A* **14**, 473–482 (2008).
58. A. J. Engler, M. A. Griffin, S. Sen, C. G. Bönnemann, H. L. Sweeney, D. E. Discher, Myotubes differentiate optimally on substrates with tissue-like stiffness. *J. Cell Biol.* **166**, 877–887 (2004).
59. R. Mestre, T. Patiño, M. Guix, X. Barceló, S. Sanchez, Design, optimization and characterization of bio-hybrid actuators based on 3D-bioprinted skeletal muscle tissue, in *Biomimetic and Biohybrid Systems. Living Machines 2019. Lecture Notes in Computer Science* (Springer-Verlag, 2018), pp. 316–320.
60. D. M. Brown, T. Parr, J. M. Brameld, Myosin heavy chain mRNA isoforms are expressed in two distinct cohorts during C2C12 myogenesis. *J. Muscle Res. Cell Motil.* **32**, 383–390 (2012).
61. U. K. Müller, J. L. van Leeuwen, Swimming of larval zebrafish: Ontogeny of body waves and implications for locomotory development. *J. Exp. Biol.* **207**, 853–868 (2004).
62. V. Mwaffo, S. Butail, M. Porfiri, In-silico experiments of zebrafish behaviour: Modeling swimming in three dimensions. *Sci. Rep.* **7**, 39877 (2017).
63. A. P. Berke, L. Turner, H. C. Berg, E. Lauga, Hydrodynamic attraction of swimming microorganisms by surfaces. *Phys. Rev. Lett.* **101**, 038102 (2008).
64. J. Simmchen, J. Katuri, W. E. Uspal, M. N. Popescu, M. Tasinkevych, S. Sánchez, Topographical pathways guide chemical microswimmers. *Nat. Commun.* **7**, 10598 (2016).
65. G. Kokot, A. Snezhko, Manipulation of emergent vortices in swarms of magnetic rollers. *Nat. Commun.* **9**, 2344 (2018).
66. G. Vizsnyiczai, G. Frangipane, S. Bianchi, F. Saglimbeni, D. Dell'Arciprete, R. Di Leonardo, A transition to stable one-dimensional swimming enhances *E. coli* motility through narrow channels. *Nat. Commun.* **11**, 2340 (2020).
67. E. M. Purcell, Life at low Reynolds number. *Am. J. Phys.* **45**, 3–11 (1977).
68. E. Lauga, T. R. Powers, The hydrodynamics of swimming microorganisms. *Rep. Prog. Phys.* **72**, 096601 (2009).
69. L. Turner, W. S. Ryu, H. C. Berg, Real-time imaging of fluorescent flagellar filaments. *J. Bacteriol.* **182**, 2793–2801 (2000).
70. A. Ghosh, P. Fischer, Controlled propulsion of artificial magnetic nanostructured propellers. *Nano Lett.* **9**, 2243–2245 (2009).
71. B. J. Williams, S. V. Anand, J. Rajagopalan, M. T. A. Saif, A self-propelled biohybrid swimmer at low Reynolds number. *Nat. Commun.* **5**, 3081 (2014).
72. R. Raman, L. Grant, Y. Seo, C. Cvetkovic, M. Gapinske, A. Palasz, H. Dabbous, H. Kong, P. P. Pinera, R. Bashir, Damage, healing, and remodeling in optogenetic skeletal muscle bioactuators. *Adv. Healthc. Mater.* **6**, 1700030 (2017).
73. H. Vandenburgh, J. Shansky, F. Benesch-Lee, V. Barbata, J. Reid, L. Thorrez, R. Valentini, G. Crawford, Drug-screening platform based on the contractility of tissue-engineered muscle. *Muscle Nerve* **37**, 438–447 (2008).
74. R. Mestre, N. García, T. Patiño, M. Guix, M. Valerio-Santiago, N. Almiñana, S. Sánchez, 3D-printed drug testing platform based on a 3D model of aged human skeletal muscle. *bioRxiv* 10.1101/2020.06.18.158659 , (2020).
75. E. Garcia, N. Lobontiu, Y. Nam, Mechanics of MEMS: A review of modeling, analysis, and design, in *Proceedings of the 2004 SPIE 5390 Smart Structures and Materials*, 26 July 2004, San Diego, CA, pp. 400–409.
76. B. Lips, R. Puers, MEMS enabled bendable and stretchable silicon circuits. *Proceedings* **2**, 837 (2018).
77. W. Jing, S. Chowdhury, M. Guix, J. Wang, Z. An, B. V. Johnson, D. J. Cappelleri, A microforce-sensing mobile microrobot for automated micromanipulation tasks. *IEEE Trans. Autom. Sci. Eng.* **16**, 518–530 (2019).
78. I. D. Johnston, D. K. McCluskey, C. K. L. Tan, M. C. Tracey, Mechanical characterization of bulk Sylgard 184 for microfluidics and microengineering. *J. Micromech. Microeng.* **24**, 035017 (2014).
79. H. Grabner, H. Bischof, On-line boosting and vision, in *2006 IEEE Computer Society Conference on Computer Vision and Pattern Recognition*, 17 to 22 June 2006, New York, NY, pp. 260–267.

Funding: M.G. thanks MINECO for the Juan de la Cierva fellowship (IJCI2016-30451), the Beatriu de Pinós Programme (2018-BP-00305), and the Ministry of Business and Knowledge of the Government of Catalonia. M.G. and G.Z. thank the Barcelona Institute of Science and Technology for the BIST Ignite Grant (ElectroSensBioBots). R.M. thanks "la Caixa" Foundation through IBEC International PhD Programme la Caixa Severo Ochoa fellowships (code LCF/BQ/SO16/52270018). T.P. thanks the European Union's Horizon 2020 research and innovation program, under the Marie Sklodowska-Curie Individual Fellowship (H2020-MSCA-IF-2018, DNA-bots). M.D.C. acknowledges funding from the European Union's Horizon 2020 research and innovation program under the Marie Skłodowska-Curie action (GA 712754), the Severo Ochoa programme (SEV-2014-0425), and the CERCA Programme/Generalitat de Catalunya. S.S. acknowledges the CERCA program by the Generalitat de Catalunya, the Secretaria d'Universitats i Recerca del Departament d'Empresa I Coneixement de la Generalitat de Catalunya through the project 2017 SGR 1148, and Ministerio de Ciencia, Innovación y Universidades (MCIU)/Agencia Estatal de Investigación (AEI)/Fondo Europeo de Desarrollo Regional (FEDER, UE) through the project RTI2018-098164-B-I00. This project was also partially funded by Agencia Estatal de Investigación (CEX2018-000789-S). This project has received funding from the European Research Council (ERC) under the European Union's Horizon 2020 research and innovation programme (grant agreement no. 866348). **Author contributions:** M.G., R.M., and T.P. conceived the study design and performed the experimental work and corresponding data collecting and analysis and manuscript writing. J.F. and G.Z. participated in the experimental procedures. The mechanical and hydrodynamical simulations on FEA were conducted by R.M. and M.D.C., respectively. M.D.C. also contributed to the manuscript writing. S.S. participated in the study design, project supervision, and manuscript writing. **Competing interests:** The authors declare that they have no competing interests. **Data and materials availability:** All data needed to evaluate the results and conclusions are included in the main text or the Supplementary Materials.

Submitted 14 September 2020
Accepted 26 March 2021
Published 21 April 2021
10.1126/scirobotics.abe7577

Citation: M. Guix, R. Mestre, T. Patiño, M. De Corato, J. Fuentes, G. Zarpellon, S. Sánchez, Biohybrid soft robots with self-stimulating skeletons. *Sci. Robot.* **6**, eabe7577 (2021).

Science Robotics

Biohybrid soft robots with self-stimulating skeletons

Maria Guix, Rafael Mestre, Tania Patiño, Marco De Corato, Judith Fuentes, Giulia Zarpellon, and Samuel Sánchez

Sci. Robot. **6** (53), eabe7577. DOI: 10.1126/scirobotics.abe7577

Science Robotics (ISSN 2470-9476) is published by the American Association for the Advancement of Science. 1200 New York Avenue NW, Washington, DC 20005. The title *Science Robotics* is a registered trademark of AAAS.